ST-ECF Instrument Science Report ACS-2006-03

Wavelength and Flux calibration of the ACS/HRC PR200L prism

S. S. Larsen, J. Walsh and M. Kümmel, March 2006

ABSTRACT

Wavelength- and flux calibrations are presented for the ACS/HRC PR200L slitless spectroscopy mode. The calibrations were derived from Cycle 13 observations of a QSO at redshift z=0.836 and a planetary nebula in the LMC (for the wavelength calibration) and two white dwarf standards (for the flux calibration), and are made available to users as configuration files for the aXe software package. Both the trace- and wavelength solutions include spatial variations across the HRC detector. The calibrations are derived for observations obtained after Nov 8th, 2004 (the aperture definitions were changed on this date) but an attempt has been made to adapt the calibrations for observations obtained before this date, as well.

Introduction

The ACS has three prisms: two in the Solar Blind Channel (PR110L and PR130L), and one in the High Resolution Channel (PR200L). The initial ground calibrations of the ACS prisms (and grism) are described in Bohlin et al. (2000). Due to the recent increase in the interest in the slitless prism spectroscopy modes on the Advanced Camera for Surveys (largely because of STIS being unavailable), an extensive effort was made in Cycle 13 to provide improved, up-to-date calibration products. This ISR describes the in-orbit wavelength- and flux calibration of the HRC PR200L prism, while the calibration of the SBC prisms (PR110L and PR130L) is discussed separately (Larsen 2006). The calibration products described here are tailored for use with the aXe spectral extraction package (Kümmel et al. 2005) and are available to users via the aXe web page (http://www.stecf.org/software/aXe).

When used with the PR200L prism, the HRC is sensitive to light with wavelengths from ~1800Å to about 10000Å, although the dispersion varies with wavelength in a highly non-linear way and in practice the useful wavelength range is restricted to ~1800Å-4000Å. However, the extended red sensitivity in combination with the rapid decrease in spectral resolution at long wavelengths results in a pile-up of flux at the red end of the spectrum, with wavelengths in the range 5000Å-10000Å being compressed into just five

pixels. As discussed below, the “red pile-up” is a major concern for observations of objects with intrinsically red spectral energy distributions, because the PSF diffraction spikes are nearly aligned with the spectral trace and can make extraction of the target spectrum difficult or impossible. Furthermore, the PSF wings contribute significantly to the background flux with a resulting degradation of the S/N. Neither of these effects is currently taken into account in the Exposure Time Calculator.

The prism aperture definitions were changed on 2004-11-08, and the trace- and wavelength solutions derived in this report are therefore valid only for observations obtained after this date. However, based on data obtained as part of earlier calibration programs, an attempt has been made to transform the calibration relations derived here to data obtained before 2004-11-08. These relations are listed here for reference, but are not discussed in detail.

Data

As for the other slitless spectroscopy modes on ACS, observations with the HRC prism generally consist of a direct image, which is used to establish the zero-point of the wavelength scale, followed by one or more exposures through the prism itself. For the wavelength calibration of the PR200L, a planetary nebula in the LMC (LMC-SMP-79) and a QSO at redshift z=0.836 (Q0037-3544) were chosen. The planetary nebula was selected to be as compact as possible. In addition, STIS spectra of the PN (kindly provided by L. Stanghellini) degraded to the spectral resolution of the PR200L indicated that the C III] 1909Å and [C II] 2325Å lines should be detectable. The QSO was selected from the catalog of Veron-Cetty & Veron (2003) such that its redshift would put the Ly α (redshifted to 2233Å) and C IV (redshifted to 2838Å) lines within the spectral range covered by the PR200L. For the flux calibration, the two white dwarf standards WD1657+343 and LDS749B were used, for which STIS spectra were kindly provided by R. Bohlin. These are the same standard stars that were used for the flux calibration of the prisms in the Solar Blind Channel (Larsen 2006).

The observations were carried out under program 10391 (P.I. Larsen) between the dates of 2004-12-20 and 2005-04-24. Each target was observed at a minimum of 5 positions across the HRC detector in order to map spatial variations in the traces, wavelength solutions and sensitivity. As illustrated in Figure 1, the PN was observed at 9 positions across the detector. Note that about 200 columns of the CCD detector (to the left) are vignetted. This vignetting is taken into account in the definition of the default prism aperture, which is centered on the unvignetted part of the detector.

A log of the observations is given in Table 1 which lists the POS-TARG offsets with respect to the default aperture center for each observation, together with the exposure times of the direct imaging and prism exposures. Direct images were taken in the F330W filter, which is the default for PR200L observations. Some objects were observed at two positions near the center of the field, separated by a small (0.014 arcsec = 0.5 pixels)

dither. This allowed a check of how sub-pixel shifts might affect the flux- and wavelength calibrations. Apart from the very short exposures in F330W for the flux standards, all exposures were split into two shorter sub-integrations in order to allow rejection of cosmic-ray hits.

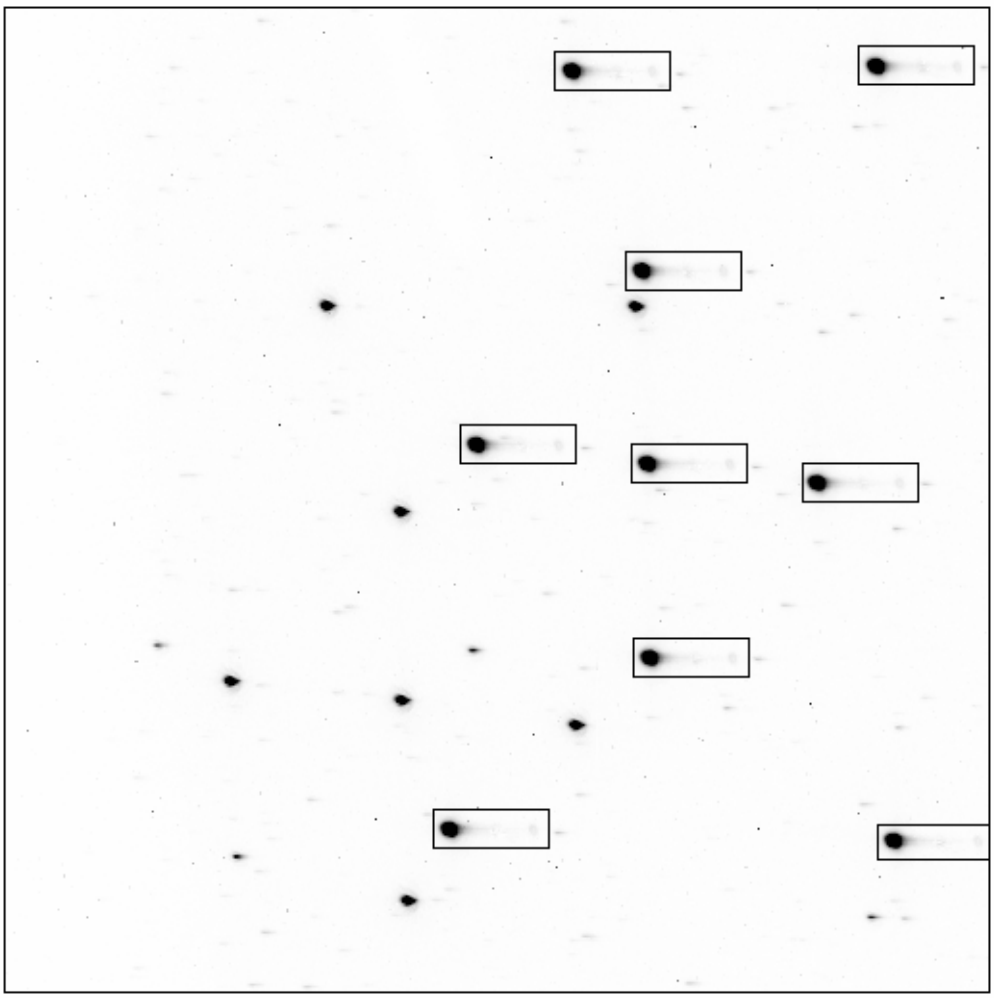

Figure 1: Sum of the 9 exposures in PR200L of LMC-SMP-79. The planetary nebula spectra are marked with boxes.

Table 1. Log of observations.

Target	POS-TARG x (arcsec)	POS-TARG y (arcsec)	T_{exp} (F330W) (s)	T_{exp} (PR200L) (s)
LDS749B	0	0	1	2x45
LDS749B	0.014	0	1	2x45
LDS749B	7	-9	1	2x45
LDS749B	-6	-10	1	2x45
LDS749B	7	11	1	2x45
LDS749B	-2	10	1	2x45
LDS749B	0	0	1	2x45
LMC-SMP-79	0	0	2x15	2x240
LMC-SMP-79	-6	-10	2x15	2x240
LMC-SMP-79	-5	0	2x15	2x240
LMC-SMP-79	-2	10	2x15	2x240
LMC-SMP-79	0	0	2x15	2x240
LMC-SMP-79	7	-9	2x15	2x240
LMC-SMP-79	5	0	2x15	2x240
LMC-SMP-79	7	11	2x15	2x240
LMC-SMP-79	0	5	2x15	2x240
LMC-SMP-79	0	-5	2x15	2x240
LMC-SMP-79	0	0.012	2x15	2x240
LMC-SMP-79	0.014	0	2x15	2x240
Q0037-3544	0	0	2x15	2x80
Q0037-3544	7	-9	2x15	2x80
Q0037-3544	-6	-10	2x15	2x80
Q0037-3544	7	11	2x15	2x80
Q0037-3544	-2	10	2x15	2x80
WD1657+343	0	0	1	2x50
WD1657+343	0.014	0	1	2x50
WD1657+343	7	-9	1	2x50
WD1657+343	-6	-10	1	2x50
WD1657+343	7	11	1	2x50
WD1657+343	-2	10	1	2x50
WD1657+343	0	0	1	2x50

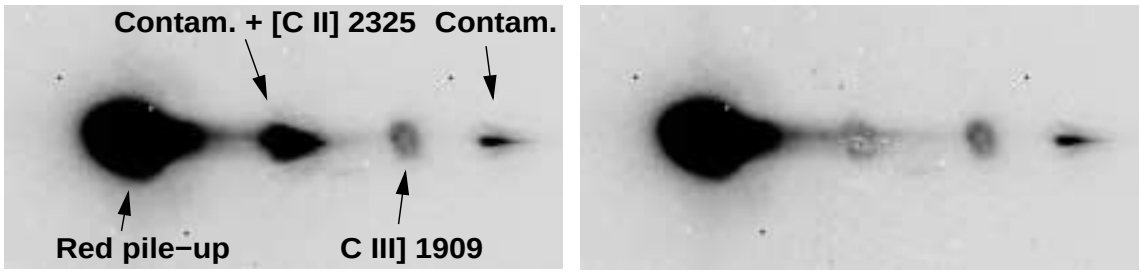

Figure 2: Left: raw prism spectrum of LMC-SMP-79. The spectrum is contaminated by two stars which by accident lie just on the spectral trace. Right: The spectrum after subtraction of one of the contaminating objects. The [C II] 2325 Å line is now clearly seen. No attempt was made to subtract the contaminant at the extreme blue end of the spectrum.

As illustrated in Figure 2, a particular problem was encountered with the observations of the planetary nebula. Two fainter objects happened to be superimposed on the trace of the prism spectrum, one of which contaminated the [C II] 2325Å line. Fortunately, it was possible to remove the contaminating object by scaling and subtracting the spectrum of another bright object with similar spectral energy distribution located elsewhere in the field. The right-hand panel in Figure 2 shows one of the prism spectra of LMC-SMP-79 after subtraction of the contaminating object and demonstrates that the [C II] line can now be measured. Based on the annular appearance of the emission lines (which are, effectively, monochromatic images of the nebula), the nebula itself is spatially resolved, while a spatially unresolved continuum from the central star is also seen.

The relative positions of the direct images and prism spectra are shown in Figure 3, where the direct image of LDS749B (scaled by a factor of 10) and the PR200L spectrum have been added. The red pile-up is clearly seen even in this fairly blue object. The prism spectrum is located to the right with respect to the direct image, with wavelength decreasing from the left towards the right. The separation between the F330W direct image and the red pile-up is about 140 pixels. Note, however, that the true deflection by the prism is much larger (about 475 pixels) and a small telescope pointing offset is automatically applied in order to cover roughly the same field in the direct imaging and spectroscopic modes.

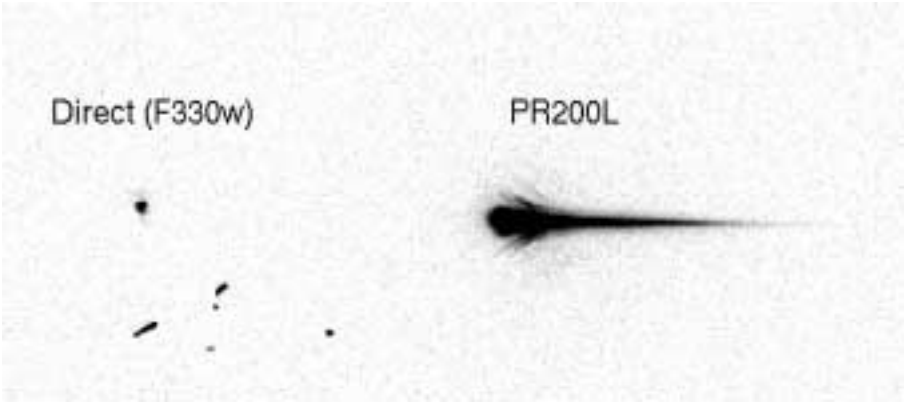

Figure 3: Sum of scaled direct image (F330W) and prism exposure of the white dwarf flux standard LDS749B. This figure shows a 350 x 150 pixels section of the image.

Initial data processing and extraction of spectra

Following standard on-the-fly pipeline processing, the first step was to define a configuration file for aXe to allow extraction of the spectra. The location of the spectral trace is defined relative to the position of the object in the direct (F330W) image, and is of the form $(Y-Y_{ref})$= DYDX_A_0 + DYDX_A_1 * $(X-X_{ref})$ + DYDX_A_2 * $(X-X_{ref})^2$ + ... where (X_{ref},Y_{ref}) are the object coordinates in the direct image and Y is the center of the trace at the distance $(X-X_{ref})$ along the detector X-axis. The coefficients DYDX_A_n are functions of the position on the detector (see the aXe manual for details).

The spectra were traced by measuring the centroid along the image columns as a function of trace distance $(X-X_{ref})$, using all observations except those of LMC-SMP-79 which were less suitable for this purpose due to the extendedness of the nebula and contamination. A linear fit was found to provide an adequate approximation to the traces, which are very nearly aligned with the detector x-axis (to within better than 1 degree). The trace description is summarized in Table 2.

The trace description was then inserted into an aXe configuration file, input object lists were created for each observation (using SExtractor), and the spectra were extracted with aXe. An extraction box width of +/-19 pixels (0.5 arcsec) was used. Since no wavelength calibration had been established at this point, a special aXe calibration file was used for this initial extraction in which the “wavelength” scale was identical to the trace distance.

Table 2. Trace description for the PR200L prism. At each position (X_{ref},Y_{ref}), the terms DYDX_A_n are described as DYDX_A_n(X_{ref},Y_{ref}) = a0n + a1n*X_{ref} + a2n*Y_{ref}.

Term	a0n	a1n	a2n
After Nov 8, 2004			
DYDX_A_0	-5.61013	0.003429	-1.25E-4
DYDX_A_1	-0.0083	-4.73E-6	-2.34E-6
Before Nov 8, 2004			
DYDX_A_0	-1.31	0.003429	-1.25E-4
DYDX_A_1	-0.0083	-4.73E-6	-2.34E-6

Wavelength calibration

The PN and QSO spectra were converted from the FITS binary table format output by aXe to IRAF 'multispec' format and the centroids of prominent emission lines in the spectra were then measured using the SPLOT task in IRAF. In the PN, both the C III] 1909Å and [C II] 2325Å lines could be measured, while Ly α (redshifted to 2233Å) and C IV (redshifted to 2838 Å) could be measured in the QSO spectrum. The C III] 1909Å line, redshifted to 3504Å, was also barely visible in the QSO spectrum, but was not used for wavelength calibration purposes as its exact location was difficult to measure due to the low spectral resolution at 3500Å and the steep slope of the prism spectrum near the red pile-up. Thus, four wavelength sampling points were available to define the dispersion solution. The usual inverse polynomial form (Bohlin et al. 2000) was assumed:

$$\lambda = \mathrm{DLD1P\_A\_1} + \mathrm{DLD1P\_A\_2}/(\Delta X - \mathrm{DLD1P\_A\_0}) + \mathrm{DLD1P\_A\_3}/(\Delta X - \mathrm{DLD1P\_A\_0})^2 + \mathrm{DLD1P\_A\_4}/(\Delta X - \mathrm{DLD1P\_A\_0})^3 + \mathrm{DLD1P\_A\_5}/(\Delta X - \mathrm{DLD1P\_A\_0})^4$$

Here, ΔX is the trace distance and the variation of the coefficients DLD1P_A_0-DLD1P_A_5 across the detector is parameterized in the same way as for the trace descriptions. With only four wavelength sampling points, it is not possible for solve for all the coefficients and the higher-order terms (DLD1P_A_3 - DLD1P_A_5) were adopted from Bohlin et al. The wavelength solutions were derived by solving directly for the full 2-D solution (see Larsen 2006 for details.). The resulting best-fit coefficients are listed in Table 3 - note that the higher-order terms are assumed to be constant across the detector area. The fits generally reproduced the reference wavelengths within better than 0.5 pixel,

corresponding to a typical accuracy of a few Å. The DLD1P_A_2 term fitted here is in reasonable agreement with the value derived by Bohlin et al. (2000), who get 83000. The table also gives approximate relations for data obtained prior to 2004-11-08. Only the zero-point of the wavelength scale has been modified, based on measurements of the C III] 1909 Å line in spectra of the PN LMC-SMP-81 observed as part of the INTERIM program (Progr. 9672, P. I. Pasquali).

Figure 4 shows the aXe-extracted spectra of the two wavelength calibration targets (note that flux calibration has also been applied). For comparison, the STIS spectrum of LMC-SMP-79 and a redshifted QSO template spectrum (Zheng et al. 1997) are also shown. The various emission features are found at the expected locations, including a hint of the C III] line in the QSO spectrum.

The wavelength scale is highly non-linear, with spectral resolution decreasing towards longer wavelengths. Figure 5 shows the wavelength and dispersion ($\Delta\lambda/\Delta$pixel) versus trace distance (left) and dispersion versus wavelength (right) for the PR200L prism. The dispersion varies from about 6Å per pixel at the blue end of the spectra (i.e. a two-pixel resolution element corresponds to $R = \lambda/\Delta\lambda \sim 150$), to ~20Å per pixel at 2500Å (R~60) and is 200Å per pixel at 4000Å (R~10). It should be noted that the behavior of the dispersion relation at wavelengths longer than 3500Å is highly uncertain, but in practice this wavelength range is likely to be of little interest to users because of the very low spectral resolution. However, the limited knowledge about the dispersion and sensitivity at long wavelengths is also likely to make a detailed modeling of the effects of the red pile-up difficult.

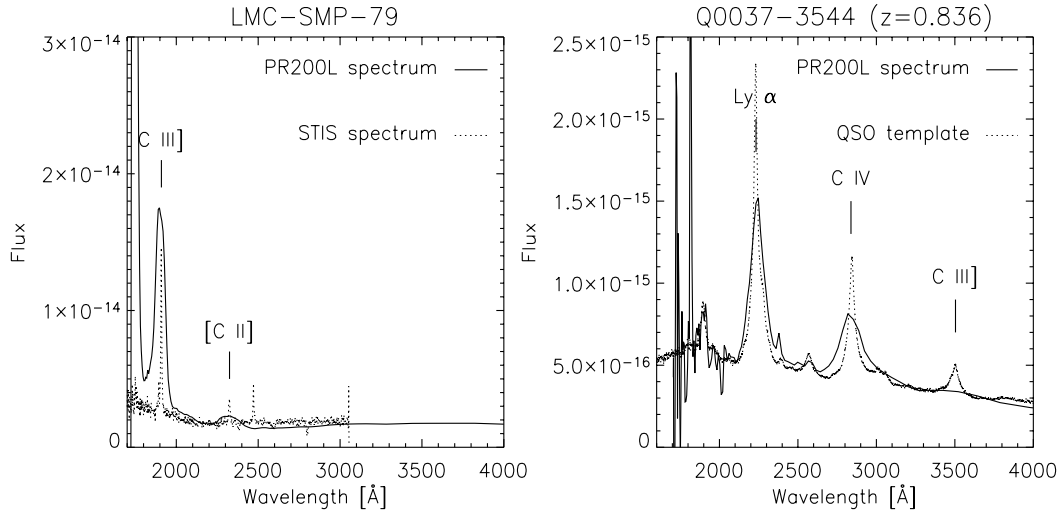

Figure 4: Comparison of aXe-extracted spectra of LMC-SMP-79 with a STIS spectrum from L. Stanghellini (left) and Q0037-3544 with a template spectrum (from Zheng et al. 1997) shifted to z=0.836 and normalized to roughly match the prism spectrum.

Table 3. Wavelength solutions for the PR200L prism. The spatial variation of the DLD1P_A_n terms is described by the a0n-a2n terms in a way analogous to that used for the trace description. Note that the DLD1P_A_3-DLD1P_A_5 terms are adopted from Bohlin et al. (2000).

	a0n	**a1n**	**a2n**
After Nov 8, 2004			
DLD1P_A_0	145.755	0.00871724	-0.0192516
DLD1P_A_1	1147.24	-0.0304151	-0.00782247
DLD1P_A_2	81100.2		
DLD1P_A_3	-828929		
DLD1P_A_4	-4.65350e+06		
DLD1P_A_5	1.68888e+08		
Before Nov 8, 2004			
DLD1P_A_0	139.077	0.00871724	-0.0192516
DLD1P_A_1	1147.24	-0.0304151	-0.00782247
DLD1P_A_2	81100.2		
DLD1P_A_3	-828929		
DLD1P_A_4	-4.65350e+06		
DLD1P_A_5	1.68888e+08		

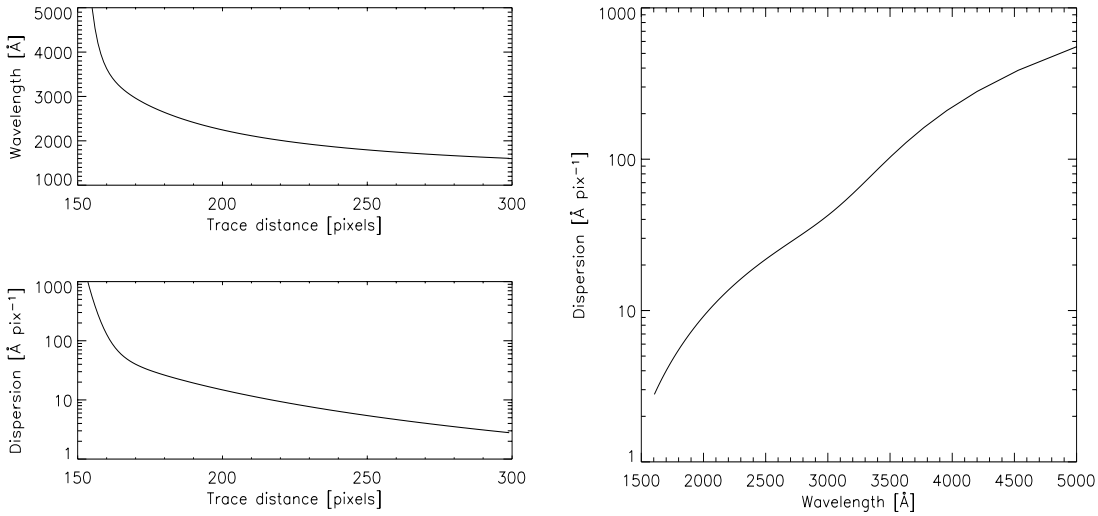

Figure 5: Left: Wavelength and dispersion vs. trace distance. Right: Dispersion vs. Wavelength.

Flux calibration

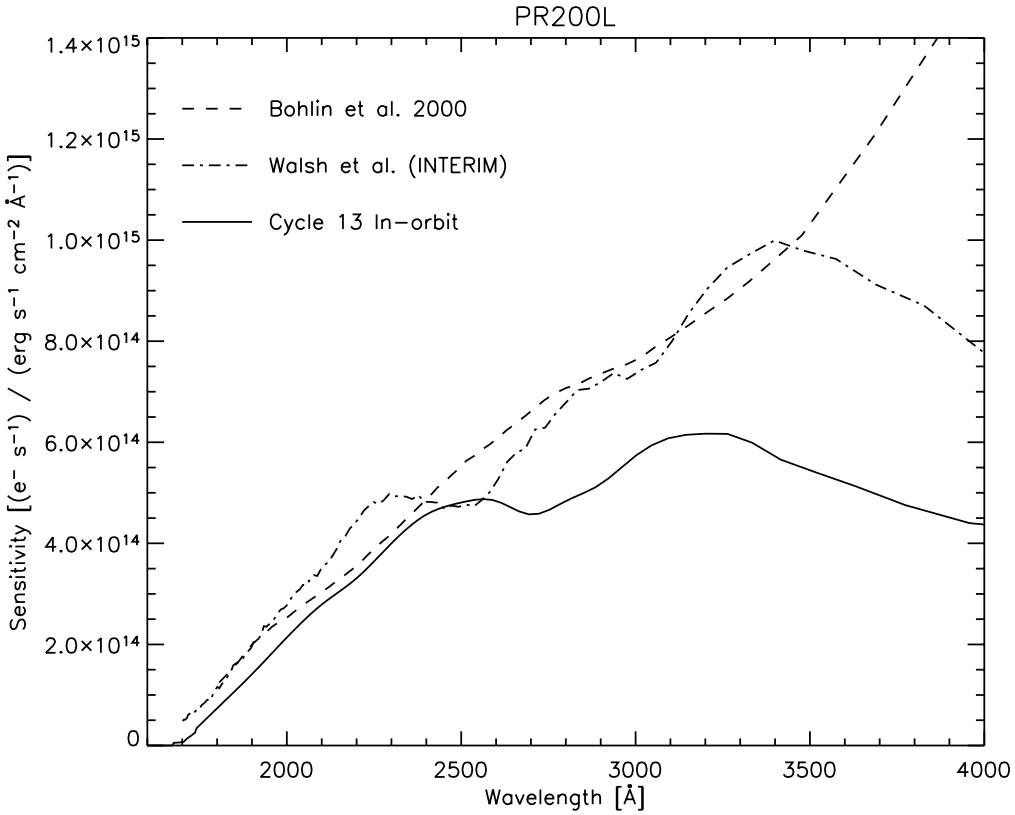

Figure 6: Comparison of sensitivity curves for the PR200L derived from the Cycle 13 in-orbit calibration (solid line), the INTERIM calibration (dotted-dashed line) and the ground calibration from Bohlin et al. 2000 (dashed curve).

Sensitivity Curves and Flat-fielding

With the wavelength solution inserted into the aXe configuration file, the spectra of the white dwarf flux standards were extracted using a box of +/-0.5 arcsec and normalized to an exposure time of 1s. The extracted spectra were then divided by STIS spectra of the standard stars, provided by R. Bohlin (see Larsen 2006 for details). Figure 6 compares the sensitivity curve derived here with the one shown in Bohlin et al. (2000), derived from the ground calibration data. A preliminary sensitivity curve, derived by J. Walsh from INTERIM (Cycle 11) calibration data, is also shown. For wavelengths shorter than 2500Å the three calibrations show reasonable agreement, while the Cycle 13 in-orbit calibration yields lower sensitivities at longer wavelengths. This is most likely related to adjustments in the wavelength solution. The sensitivity curve derived from the Cycle 13 data is given in tabular form in Table 4.

The pipeline processing of PR200L spectroscopic exposures includes flat-fielding to remove pixel-to-pixel sensitivity variations (Bohlin & Hartig 2002). Comparison of the extracted prism spectra of the flux standards with the STIS reference spectra (Figure 7) shows that the pipeline processing appears to be mostly appropriate, except for spectra located in the lower right-hand corner of the detector where the fluxes are underestimated by about 10%. The aXe package supports the use of a flat-field cube in order to correct for sensitivity variations as a function of both wavelength and position on the detector. A flat-field cube has been constructed for the PR200L, using imaging exposures in a selection of broad-band filters (see Walsh & Pirzkal 2005 for details), but application of the flat-field cube would cause the pixel-to-pixel sensitivity corrections to be applied twice, which is clearly not desirable. In order to avoid this, a modified version of the PR200L flat-field cube was constructed by dividing the first-order (wavelength-independent) term with the pipeline flatfield. The resulting image, which is effectively an L-flat, indeed shows a drop in sensitivity on the order of 10% towards the lower right-hand corner of the detector. As shown in the left-hand panels of Figure 7, application of this extra flat-field correction does help to remove the systematic differences in the fluxes for objects located at various positions on the detector.

Apart from this, the extracted and calibrated spectra show good agreement with the standard spectra at least down to wavelengths of 1800Å, below which the sensitivity drops steeply. For the wavelength range 1800Å-3500Å, it appears that a flux calibration accurate to about 5% is possible over most of the detector area.

In order to quantify the effect of sub-pixel offsets and binning on the flux calibration, exposures were obtained at small (0.5 pixels) dither offsets for the central pointings. Figure 8 compares the PR200L spectra (central pointing only) for the two flux standards, including both the default (POS-TARG = 0) and offset (POS-TARG x = 0.5 pixels) positions. The spectra were extracted using the appropriate direct images, i.e. with proper account for the 0.5 pixels offset. It is clear from the figure that sub-pixel shifts are not a major source of concern for PR200L prism observations.

Finally, from the sensitivity curves it is straight forward to compute the total system throughput for the PR200L spectroscopy mode, shown in Figure 9. This peaks at about 9% between 2400Å and 3500Å, compared to a total OTA (Optical Telescope Assembly) throughput of 60%.

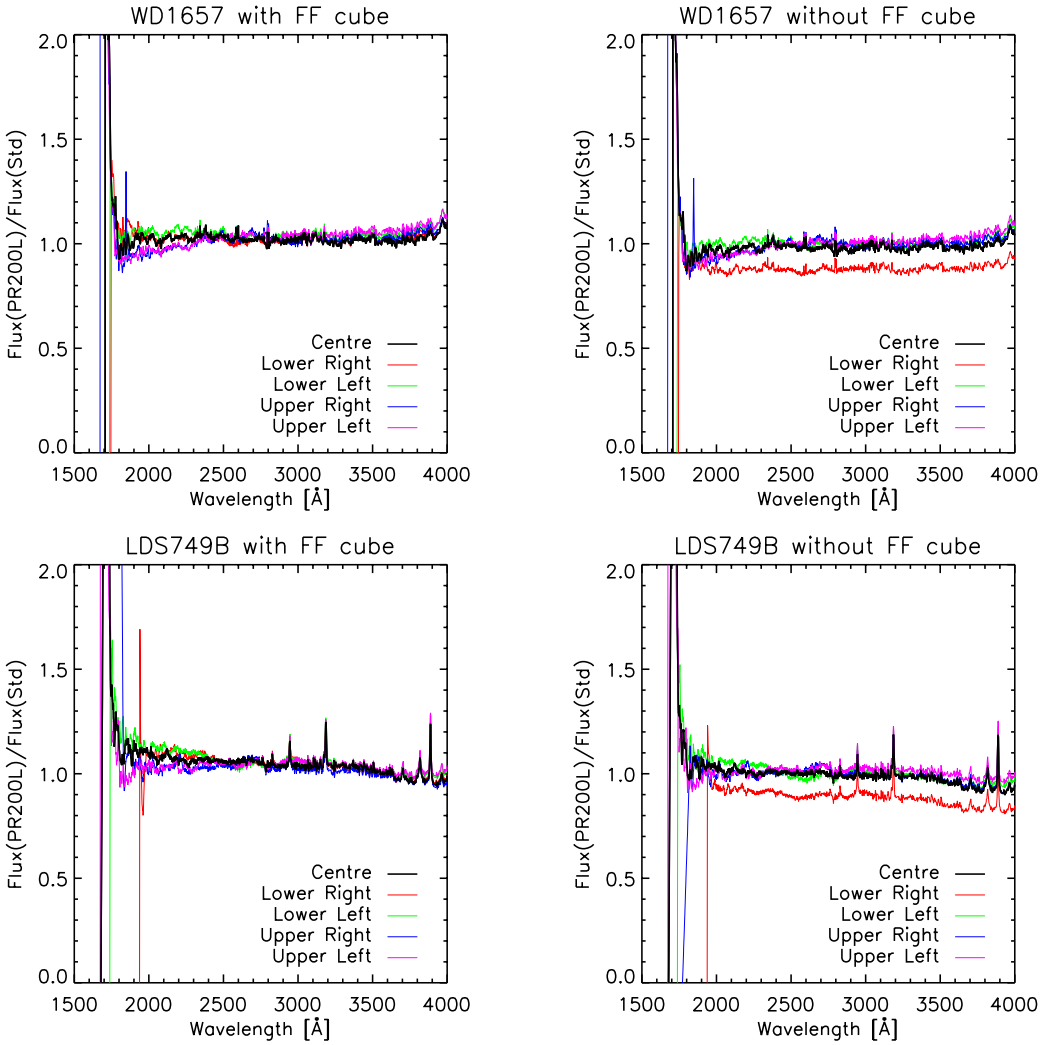

Figure 7: Comparison of the aXe-extracted prism spectra of the two flux standards with the reference spectra. In each panel, the ratio of aXe/standard is shown for 5 different positions on the HRC detector. In the left-hand panels, an L-flat derived from the wavelength-independent term in a flat-field cube was used to remove large-scale sensitivity variations.

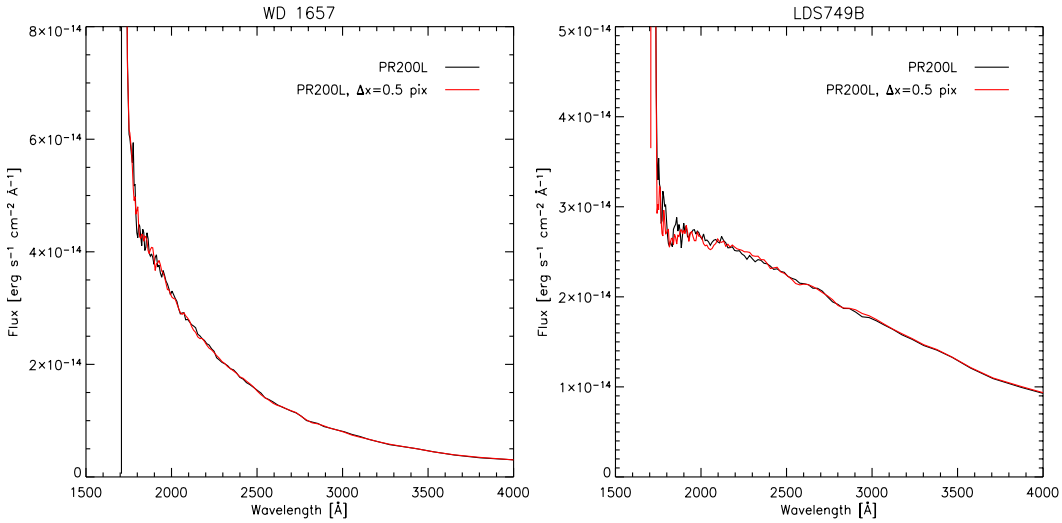

Figure 8: aXe extracted PR200L spectra of the two flux standards. Observations were obtained at two dither positions separated by 0.5 pixels in the x-direction. No systematic difference is apparent between the two dither positions.

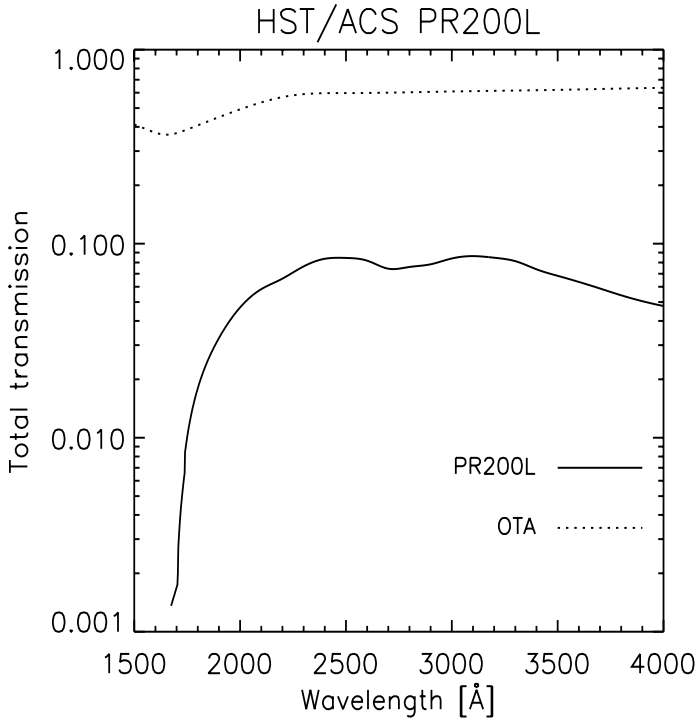

Figure 9: Total throughput of the PR200L, derived from the sensitivity curve. For comparison, the throughput of the OTA is also shown.

Aperture corrections

Like the ACS (and WFPC2) photometric calibrations, the standard sensitivity file for the HRC PR200L refers to an aperture size of +/-0.5 arcsec. However, for some applications it may be desirable to use other aperture sizes. In order to quantify the loss of flux for different aperture sizes, spectra of the flux standards were extracted for a range of aperture sizes and normalized to the fluxes in the default aperture. The normalized flux as a function of aperture size is shown in Figure 10 for three different wavelength ranges (2000Å-2400Å, 2500Å-3000Å, and 3000Å-4000Å). The data shown in Figure 10 are also listed in Table 5. It should be noted that these corrections are only valid for point sources, and will typically be larger for extended objects.

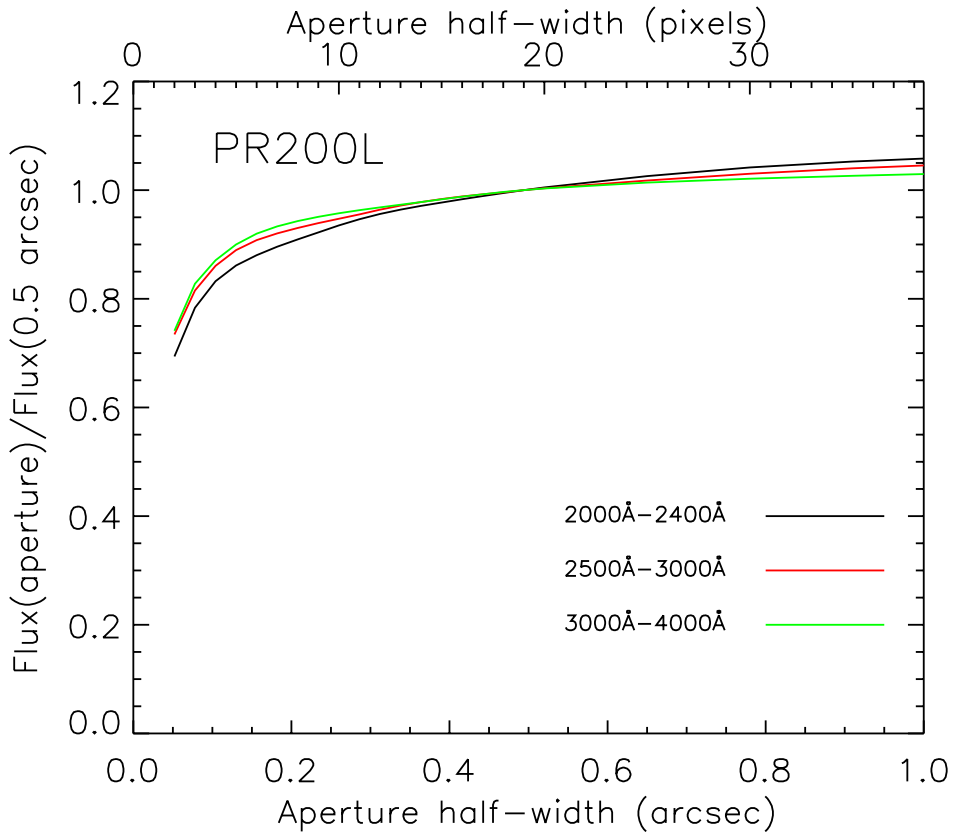

Figure 10: Flux as a function of aperture half-width in pixels and arcsec for a point source. Three different wavelength ranges are shown. The fluxes are normalized to unity for an aperture of +/-0.5 arcsec (+/-19 pixels).

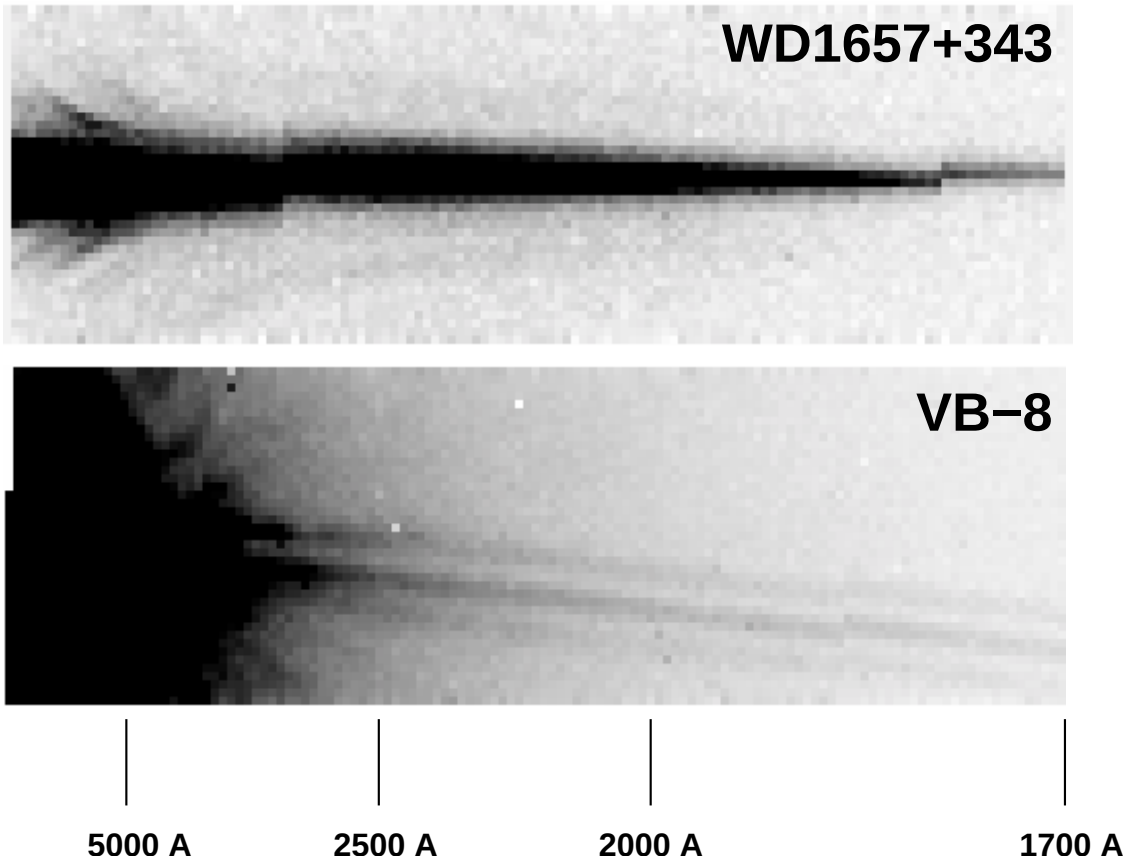

Figure 11: Stamp images produced by aXe for the white dwarf standard WD1657+343 (top) and the M7 star VB-8. The wavelength scale is indicated at the bottom of the plot. The discontinuities in the trace are artifacts.

A final note on the red pile-up

The red pile-up is always noticable in PR200L spectra, but it can be dramatic for intrinsically red objects. As an illustration of this, Figure 11 shows the aXe stamp images of two objects: one of the white dwarf flux standards (WD1657+343), and an M7 star observed as part of program 10740 (P.I. Bohlin). For both stars, the stamp images correspond to the +/-0.5” wide box used for all observations in this report. The wavelength scale is indicated at the bottom of the figure. Note that the wavelength solution diverges at a trace distance of about 150 pixels (see Table 4 and Figure 5) - only pixels at greater trace distances are shown in Figure 11.

While the spectrum of the white dwarf (top panel) is well centered on the stamp image and can be traced over the full wavelength range, the stamp image of the M7 star is completely dominated by the red pile-up, and no spectral trace is visible. Instead, only the diffraction spikes from the point spread function are seen. Clearly, it will be very difficult to extract useful information from such data.

Further study will be needed to quantify appropriate steps to optimal use of PR200L observations of red targets. The diffraction spikes are near the expected spectrum position at long wavelengths, but deviate significantly below 2500Å. It may be possible to shift and scale diffraction spikes from a broad-band filter such as F606W in order to subtract this contamination to first order. Will scaling by the sum over the full red pile-up suffice? By comparing archive spectra of O, F and M stars it should be possible to quantify this. By this or similar means it should be possible to define the range of spectral energy distributions, and blue to red flux ratios for which PR200L observations provide useful spectra.

Summary

This ISR has presented in-orbit wavelength and flux calibrations for the HRC PR200L prism. The wavelength scale is accurate to better than 1 pixel, corresponding to a few Å at the blue end (~2000Å) and about 10Å at intermediate wavelengths (~2500Å-3000Å). At longer wavelengths the wavelength solution becomes highly nonlinear and increasingly uncertain, although for most users, observations at wavelengths longer than 3500-4000Å are likely to be of little interest due to the very low spectral resolution there. However, the limited knowledge about the wavelength solution at long wavelengths may cause limitations for attempts to model the detailed behavior of the “red pile-up”, which is a major concern for objects with intrinsically red spectral energy distributions.

The flux calibration derived here is expected to be accurate to about 5% over the wavelength range 1800Å-3000Å and across most of the field of view. The trace, wavelength and flux calibrations presented here are implemented in the standard file formats used by the aXe package, and are available for download via the aXe web page (http://www.stecf.org/software/aXe).

Acknowledgements

We thank R. Bohlin, R. Gilliland, J. Maíz-Apellániz and K. Sembach for helpful comments on this ISR.

References

Bohlin, R. C, Hartig, G., & Boffi, F. R., 2000, *Predicted Sensitivity and Dispersion of the Prisms and Grism*, ISR ACS 2000-001

Bohlin, R. C., & Hartig, G., 2002, *HRC and WFC Flat Fields: Dispersors, Anomalies, and Photometric Stability*, ISR ACS 2002-004

Kümmel, M., Larsen, S. S., & Walsh, J. R., 2005, *Slitless Spectroscopy with the Advanced Camera for Surveys*, 2005 HST Calibration Workshop, STScI (astro-ph/0512102)

Larsen, S. S., 2006, *Wavelength and Flux Calibration of the ACS/SBC PR110L and PR130L Prisms*, ACS ISR 2006-02
Pasquali, A., Pirzkal, N., Larsen, S. S., et al., 2005, PASP, in press (astro-ph/0510428)
Veron-Cetty, M. P., & Veron, P., 2003, A&A, 412, 399
Walsh, J. R., & Pirzkal, N., 2005, *Flat-field and Sensitivity Calibration for G800L Slitless Spectroscopy Modes*, ACS ISR 05-02
Zheng, W., Kriss, G. A., Telfer, R. C., et al., 1997, ApJ, 475, 469

Table 4. Wavelength, dispersion and sensitivity versus trace distance. This table is for an object centered on the HRC detector (X,Y) = (512, 512). Sensitivity is in units of (e- s^{-1}) / (erg s^{-1} cm^{-2} $Å^{-1}$). Note that the behavior of the wavelength scale and sensitivity curve are highly uncertain at wavelengths longer than about 3500Å.

$X-X_{ref}$ [pixels]	Wavelength [Å]	Dispersion [Å/pix]	Sensitivity
151	10745	3206	1.68461e+15
152	8228.3	1949	1.03066e+15
153	6668.7	1234	7.02722e+14
154	5664.2	810.5	5.67560e+14
155	4993.7	550.8	4.88041e+14
156	4530.9	386.9	4.44842e+14
157	4200.9	280.6	4.24429e+14
158	3957.9	210.0	4.40013e+14
159	3773.4	162.0	4.75608e+14
160	3629.0	128.8	5.13446e+14
161	3512.6	105.3	5.41509e+14
162	3416.3	88.30	5.65624e+14
163	3334.5	75.81	5.99089e+14
164	3263.6	66.44	6.16580e+14
165	3200.9	59.27	6.16981e+14
166	3144.5	53.68	6.14729e+14
167	3093.2	49.22	6.07829e+14
168	3045.8	45.61	5.93894e+14
169	3001.8	42.61	5.74116e+14
170	2960.4	40.09	5.50477e+14
171	2921.5	37.93	5.27924e+14
172	2884.5	36.05	5.10771e+14
173	2849.3	34.39	4.98966e+14
174	2815.7	32.90	4.88867e+14
175	2783.4	31.55	4.77668e+14
176	2752.5	30.32	4.66371e+14
177	2722.8	29.19	4.58609e+14

$X-X_{ref}$ [pixels]	Wavelength [Å]	Dispersion [Å/pix]	Sensitivity
178	2694.1	28.14	4.57360e+14
179	2666.5	27.16	4.63054e+14
180	2639.8	26.25	4.71943e+14
181	2614.0	25.38	4.80491e+14
182	2589.0	24.56	4.85867e+14
183	2564.8	23.79	4.87381e+14
184	2541.4	23.06	4.86241e+14
185	2518.7	22.36	4.83546e+14
186	2496.7	21.69	4.80206e+14
187	2475.3	21.05	4.76701e+14
188	2454.5	20.44	4.72758e+14
189	2434.4	19.86	4.68047e+14
190	2414.8	19.30	4.62290e+14
191	2395.8	18.77	4.55259e+14
192	2377.3	18.25	4.46907e+14
193	2359.3	17.76	4.37511e+14
194	2341.8	17.28	4.27339e+14
195	2324.7	16.82	4.16617e+14
196	2308.1	16.38	4.05542e+14
197	2291.9	15.96	3.94282e+14
198	2276.2	15.55	3.83023e+14
199	2260.8	15.16	3.71968e+14
200	2245.9	14.78	3.61291e+14
201	2231.3	14.41	3.51140e+14
202	2217.0	14.06	3.41640e+14
203	2203.2	13.72	3.32897e+14
204	2189.6	13.39	3.24979e+14
205	2176.4	13.07	3.17771e+14
206	2163.5	12.76	3.11089e+14
207	2150.8	12.47	3.04773e+14
208	2138.5	12.18	2.98681e+14
209	2126.5	11.90	2.92692e+14

X-X_{ref} [pixels]	Wavelength [Å]	Dispersion [Å/pix]	Sensitivity
210	2114.7	11.63	2.86698e+14
211	2103.2	11.37	2.80605e+14
212	2092.0	11.12	2.74341e+14
213	2081.0	10.88	2.67908e+14
214	2070.2	10.64	2.61349e+14
215	2059.7	10.41	2.54700e+14
216	2049.4	10.19	2.47992e+14
217	2039.3	9.98	2.41257e+14
218	2029.4	9.77	2.34519e+14
219	2019.8	9.56	2.27799e+14
220	2010.3	9.37	2.21117e+14
221	2001.0	9.18	2.14491e+14
222	1991.9	8.99	2.07936e+14
223	1983.0	8.81	2.01464e+14
224	1974.3	8.64	1.95088e+14
225	1965.8	8.47	1.88815e+14
226	1957.4	8.31	1.82655e+14
227	1949.1	8.15	1.76615e+14
228	1941.1	7.99	1.70702e+14
229	1933.2	7.84	1.64920e+14
230	1925.4	7.69	1.59274e+14
231	1917.8	7.55	1.53767e+14
232	1910.3	7.41	1.48402e+14
233	1903.0	7.27	1.43183e+14
234	1895.7	7.14	1.38109e+14
235	1888.7	7.01	1.33177e+14
236	1881.7	6.89	1.28374e+14
237	1874.9	6.77	1.23696e+14
238	1868.2	6.65	1.19132e+14
239	1861.6	6.53	1.14674e+14
240	1855.1	6.42	1.10318e+14
241	1848.8	6.31	1.06053e+14

$X-X_{ref}$ [pixels]	Wavelength [Å]	Dispersion [Å/pix]	Sensitivity
242	1842.5	6.20	1.01877e+14
243	1836.3	6.10	9.77819e+13
244	1830.3	6.00	9.37635e+13
245	1824.3	5.90	8.98168e+13
246	1818.5	5.80	8.59375e+13
247	1812.7	5.71	8.21213e+13
248	1807.1	5.61	7.83641e+13
249	1801.5	5.52	7.46628e+13
250	1796.0	5.43	7.10140e+13
251	1790.6	5.35	6.74162e+13
252	1785.3	5.26	6.38695e+13
253	1780.1	5.18	6.03732e+13
254	1775.0	5.10	5.69264e+13
255	1769.9	5.02	5.35295e+13
256	1764.9	4.95	5.01816e+13
257	1760.0	4.87	4.68821e+13
258	1755.2	4.80	4.36306e+13
259	1750.4	4.73	4.04265e+13
260	1745.7	4.66	3.72692e+13
261	1741.1	4.59	3.41582e+13
262	1736.6	4.52	2.52171e+13
263	1732.1	4.46	2.29087e+13
264	1727.6	4.39	2.06372e+13
265	1723.3	4.33	1.84021e+13
266	1719.0	4.27	1.62027e+13
267	1714.7	4.21	1.40385e+13
268	1710.6	4.15	1.19092e+13
269	1706.4	4.09	8.46025e+12
270	1702.4	4.03	6.68543e+12
271	1698.4	3.98	6.45047e+12

Table 5. Flux versus extraction box half-width for the PR200L, relative to an extraction box half-width of 0.5 arcsec. The corrections are listed for three different wavelength ranges.

Half-width (pixels)	Half-width (arcsec)	Flux/ Flux(0.5”) [2000-2400Å]	Flux/ Flux(0.5”) [2500-3000Å]	Flux/ Flux(0.5”) [3000-4000Å]
2	0.052	0.694	0.734	0.741
3	0.078	0.783	0.815	0.828
4	0.104	0.832	0.861	0.871
5	0.130	0.861	0.890	0.900
6	0.156	0.880	0.908	0.920
7	0.182	0.896	0.920	0.933
8	0.208	0.909	0.930	0.943
9	0.234	0.922	0.939	0.951
10	0.260	0.935	0.947	0.957
11	0.286	0.946	0.955	0.963
12	0.312	0.956	0.964	0.968
13	0.338	0.964	0.972	0.973
14	0.364	0.971	0.978	0.978
15	0.390	0.977	0.984	0.983
16	0.416	0.983	0.988	0.988
17	0.442	0.989	0.992	0.992
18	0.468	0.995	0.996	0.997
19	0.494	1.000	1.000	1.000
20	0.520	1.005	1.003	1.003
25	0.650	1.026	1.018	1.014
30	0.780	1.042	1.030	1.021
35	0.910	1.053	1.040	1.026
40	1.040	1.061	1.048	1.031